PERGAMON

International Journal of Solids and Structures 37 (2000) 7281–7305

INTERNATIONAL JOURNAL OF SOLIDS and STRUCTURES

www.elsevier.com/locate/ijsolstr

Interfacial failures in a compressive shear strength test of glass/polymer laminates

P. Rahul-Kumar [a,*], A. Jagota [b], S.J. Bennison [b], S. Saigal [a]

[a] *Department of Civil and Environmental Engineering, Carnegie Mellon University, Pittsburgh, PA 15213, USA*
[b] *CR&D, The DuPont Company, Experimental Station, Wilmington, Delaware, DE 19880-0356, USA*

Received 16 August 1999; in revised form 15 February 2000

Abstract

A computational method for interfacial failure modeling in composite material systems using cohesive elements is developed. This method is based on phenomenological cohesive zone models implemented within an implicit finite element framework as cohesive elements. Dynamic 2D and 3D cohesive elements have been developed and are used to simulate a compressive shear strength (CSS) test. The CSS test is employed in the polymer industry to measure polymer/substrate adhesion. The computational framework is first verified against existing analytical solutions for dynamic crack growth in double cantilever beam specimens. The phenomenon of stable crack growth followed by unstable crack growth observed in the CSS experiment is simulated. Various crack growth behaviors, obtained for different sizes of the initial pre-flaw along the interface, are studied. The phenomenon of dynamic crack "pop-in", consisting of dynamic crack growth followed by crack arrest and stable crack growth, is investigated. The influence of the cohesive zone model parameters on crack "pop-in" as well as stability of crack growth are studied. A 3D dynamic simulation of a square plan form of CSS test is performed. The 3D analyses reveal the mixed-mode behavior in crack front growth along the interface and local "pop-through" of the crack front near the free edge of the CSS test specimen.

Keywords: Fracture; Cohesive zone models; Finite elements; Cohesive elements; Dynamic crack growth; Crack pop-in; Polymers

1. Introduction

Composite multi-layered material systems are being employed increasingly in high-performance engineering applications. The mechanical performance and reliability of these material systems is directly related to the strength or fracture toughness of their interfaces under quasi-static and dynamic loading conditions. Complexities in the mechanics of interfacial cracks make the definition and extraction of fracture parameters a formidable task, even for linear elastic materials. Much of the literature on this topic, reviewed briefly below, is based on asymptotic analyses of near-crack-tip fields. Crack propagation in

* Corresponding author. Fax: +1-412-268-7813.
E-mail addresses: rahulkumarp@ornl.gov (P. Rahul-Kumar), saigal@cmu.edu (S. Saigal).

0020-7683/00/$ - see front matter
PII: S0020-7683(00)00199-2

polymers and polymer interfaces is often accompanied by nonlinear mechanical behavior and attendant energy loss at many length scales. These range from bond rupture at the finest length scale, through crazing, chain pull-out and cavitation at the meso scale, to bulk inelastic losses. Studies of interfacial fracture in the presence of such mechanical characteristics are few and difficult to analyze using conventional energy release rate or stress-intensity approaches to fracture mechanics. Recent developments of the cohesive zone approach to fracture offer an alternative method for treating such a material complexity in interfacial fracture. When implemented as cohesive elements in a computational finite element code, this approach allows one to analyze polymer fracture governed by large inelastic deformation and dissipation at many length scales. The main aim of this paper is to present the development of the cohesive element technique for polymer interfacial fracture in the context of implicit finite element computations.

The use of cohesive zone models was pioneered by Barenblatt (1962), Dugdale (1960), for fracture in elastic, elastic–plastic materials and Knauss (1973), Schapery (1975) for fracture in viscoelastic materials. The cohesive zone model is specified as a force-separation relationship. For linear elastic materials, the integrated work of separation specifies the fracture resistance, Γ_0. However, the cohesive zone model involves additional parameters, e.g., a characteristic opening displacement or peak stress. This additional parameter governs the cohesive zone length that defines an extended crack-tip region representing various fracture processes. Cohesive zone modeling of fracture has recently been used in a finite element framework by, among others, Needleman (1990a,b), Tvergaard and Hutchinson (1992), Xu and Needleman (1994, 1995, 1996), Camacho and Ortiz (1996) and Espinosa et al. (1998) for studying fracture in elastic–plastic and brittle solids. Needleman (1990a,b) employed a cohesive zone interface model within an implicit static solution procedure to investigate numerically the problem of decohesion between an elastic–viscoplastic block and a rigid substrate. Xu and Needleman (1995, 1996) used cohesive elements within a 2D explicit solution scheme to perform a numerical study of dynamic interfacial crack growth along and away from the interface in a bimaterial system.

Several studies of interfacial fracture in the literature are based on energy release rate and stress intensity factor methods. Several researchers have proposed phenomenological interfacial fracture toughness criteria as a function of the relative amounts of mode I and mode II conditions at the interface (Hutchinson and Suo, 1992). The majority of the work on interfacial fracture assumes that crack-tip nonlinear zones are small and contained within the elastic stress fields characterized by stress intensity factors, ''small scale yielding''. It is not clear that these approaches can be applied to analyze interfacial fracture experiments involving nonlinear material behaviors, finite strains, and dynamic crack propagation conditions. An alternative approach is the use of cohesive zone models to simulate interfacial failure. In a recent study, Swadener and Liechti (1998) used a cohesive zone model for studying interfacial failures in epoxy/metal interfaces. They demonstrated that a cohesive zone model could successfully account for the variation in the experimentally measured macroscopic fracture toughness as a function of mode mixity. A computational method employing cohesive zone models through cohesive elements can be attractive for studying interfacial failures as it would obviate the need for several simplifying assumptions as required with the energy release rate and stress intensity factor methods.

There are several advantages to using cohesive elements for computational modeling of interfacial fracture. The work required to separate the interface is specified directly by the cohesive model. Crack propagation in elastic materials is consistent with criteria based on critical energy release rate or stress intensity factors. However, the cohesive zone approach applies naturally to crack propagation accompanied by nonlinear deformation, obviating the need for separate crack initiation and propagation criteria based on the surrounding displacement and stress field solutions. The specification of fracture and bulk constitutive behavior is independent. Therefore, the influence of bulk material response on globally measured fracture behavior can be separated from the direct effect of changing fracture mechanism. This is particularly useful in treating the effects of specimen geometry to extract a material-based fracture resistance. The implementation of cohesive elements is independent of the elements that represent the bulk. As a

consequence, one can handle different types of inelasticity, e.g., elasto-plastic, rate-sensitive viscoelastic/viscoplastic, and different simulation procedures (static, dynamic, etc.)

The emphasis of the analyses presented here is to demonstrate the above mentioned advantages of the cohesive element technique. This is achieved by using the technique to study crack growth in a compressive shear strength (CSS) test. The CSS test is used in the polymer industry to extract interfacial adhesion between polymer and glass in glass/polymer laminates. Using the CSS test as a vehicle, various crack growth behaviors along the glass/polymer interface under stable and unstable crack growth conditions are simulated. The phenomenon of dynamic crack "pop-in" along the glass/polymer interface is also investigated. The need for modeling stable crack growth under quasi-static conditions and unstable crack growth under dynamic conditions requires the use of an implicit dynamic solution framework. In the CSS test, the glass/polymer interface experiences combined compression and shear. Cohesive elements experiencing compression during the deformation process require numerical techniques that prevent the inter-penetration of the cohesive element surfaces. Contact algorithms have been used in the literature (Camacho and Ortiz, 1996; Espinosa et al., 1998) to prevent inter-penetration of cohesive surfaces within an explicit finite element solution framework. The use of such contact algorithms within the implicit dynamic finite element solution framework would be computationally prohibitive as it would lead to computational costs associated with the solution of momentum balance equations. These computations are in addition to those associated with the Newton–Raphson iterations for the solution of the nonlinear finite element equations to establish equilibrium. In this study a penalty formulation is used within the cohesive element framework to prevent inter-penetration of cohesive surfaces under compression.

2. Compressive shear strength test description and analysis background

A schematic of the experimental setup of the CSS test is shown in Fig. 1. The specimen used in the test is a three ply glass/polymer/glass composite laminate that may be held at different angles between a lower trolley which is free to translate in the horizontal direction and an upper block that moves vertically under applied load. The specimen experiences a combined state of compression and shear under this loading. A common use of this experiment is to measure adhesion between glass and poly(vinyl butyral) (Butacite®), a polymer used in architectural glazing and automotive safety glass. The polymer undergoes large rubber-like

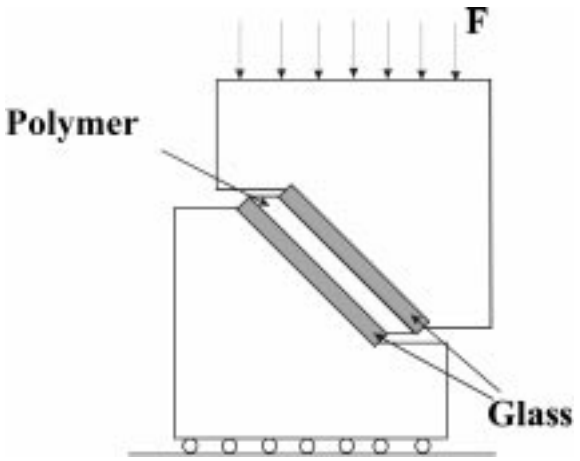

Fig. 1. Schematic drawing of the 45° CSS test.

shear strains, which contributes to the bulk viscous dissipation. By recording the force and displacement of the loading arm the shear strain and the macroscopic average shear stress across the specimen are obtained. Fig. 2(a) shows the specimen prior to application of strain. Under monotonic straining, for "low" levels of adhesion between polymer and glass surfaces, a stable crack nucleates at the free edge of specimen along one of the glass/polymer interfaces. This crack undergoes stable growth along the interface, Fig. 2(b), followed by a final instability and unstable crack growth at a critical level of applied macroscopic shear strain. Stable crack growth along the interface occurs predominantly in an opening mode by peeling of the polymer from the glass surface until the instant of instability. The following unstable crack growth is characterized by large amounts of sliding along the glass/polymer interface. Experimental macroscopic shear stress and shear strain curves obtained in the CSS test for different strain rates are shown in Fig. 3. For a given rate of straining the measured macroscopic stress first increases with increasing shear strain,

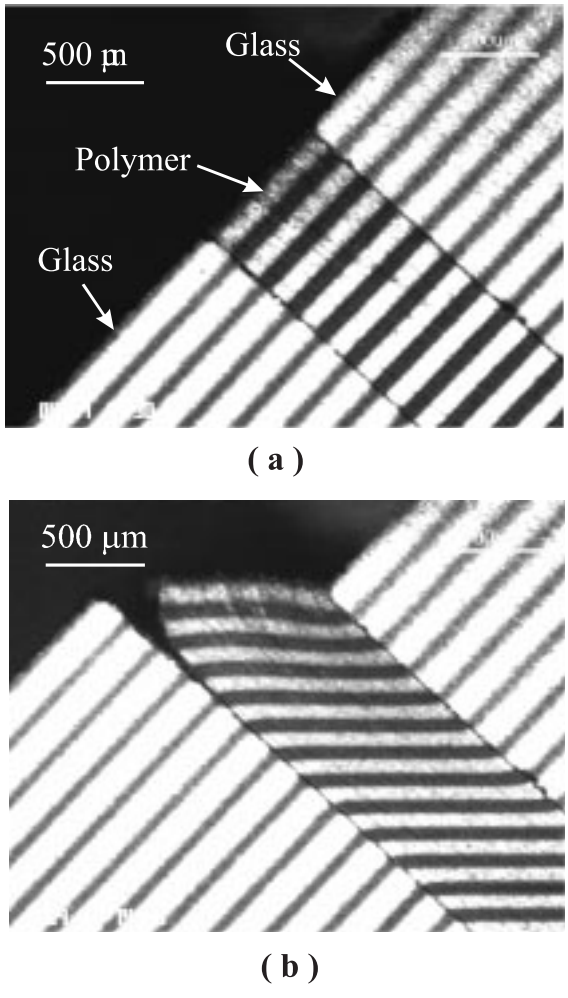

Fig. 2. (a) Micrograph showing a three-ply laminate near free corner. Striped markings on the surface have been produced by evaporating a thin gold film through a mask. These aid in visualizing the deformation of the specimen during the experiment. (b) Micrograph showing a stable crack along the glass/polymer interface just prior to the instability at which the interface fails.

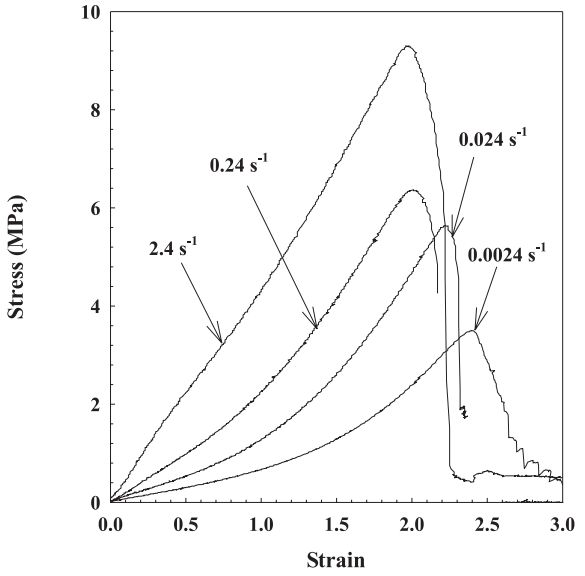

Fig. 3. Experimental macroscopic shear stress and shear strain measured in the CSS test for different strain rates.

during which stage stable crack propagation occurs, next attains a maximum, and finally drops suddenly due to the unstable crack growth caused by the failure of the interface.

The data shown in Fig. 3 indicate that crack growth occurs in the presence of large, rate-dependent material deformation. If one ignores rate dependence, bulk constitutive behavior can be modeled well by hyperelasticity, which allows an energy release rate analysis. The normalized energy release rate, $\Gamma^* = \Gamma/Uh$, as a function of normalized crack length, $a^* = a/h$, for crack growth along the glass/polymer interface in a CSS test has been obtained (Jagota et al., 2000) for different levels of applied shear strains, γ. Here, Γ is the energy release rate, U, the strain energy density in the polymer material under simple shear strain, γ, h, the polymer thickness, and a, the crack length. A typical energy release rate curve is shown in Fig. 4 for the case of where the specimen is held at an angle of 45° with an applied shear strain, $\gamma = 0.5$. For an interface of strength, $\Gamma_0^* = \Gamma_0/Uh$, where Γ_0 is the fracture energy, and, with a flaw of size, a_0^*, the equilibrium crack location, a_e^*, is given by

$$\Gamma^*(a^*)|_{a_e^*} = \Gamma_0^*. \tag{1}$$

This location is stable if

$$\left.\frac{\mathrm{d}\Gamma^*(a^*)}{\mathrm{d}a^*}\right|_{a_e^*} < 0. \tag{2}$$

The following four different crack growth behaviors are predicted:

1. Small crack limit, $a_0^* < a_1^*$: the flaw remains stationary until, $\Gamma^* = \Gamma_0^*$, at which point the flaw undergoes unstable crack growth.
2. Short crack regime, $a_1^* < a_0^* < a_2^*$: the flaw remains stationary until, $\Gamma^* = \Gamma_0^*$. The flaw then "pops-in" and is arrested on the descending part of the energy release curve. It then undergoes stable crack growth, and eventually experiences unstable growth when $\Gamma^* = \Gamma_0^* = \Gamma_3^*$.
3. Intermediate crack regime, $a_2^* < a_0^* < a_3^*$: crack growth initiates when, $\Gamma^* = \Gamma_0^*$. Subsequent crack growth is stable until $\Gamma^* = \Gamma_0^* = \Gamma_3^*$, beyond which the crack propagates unstably.

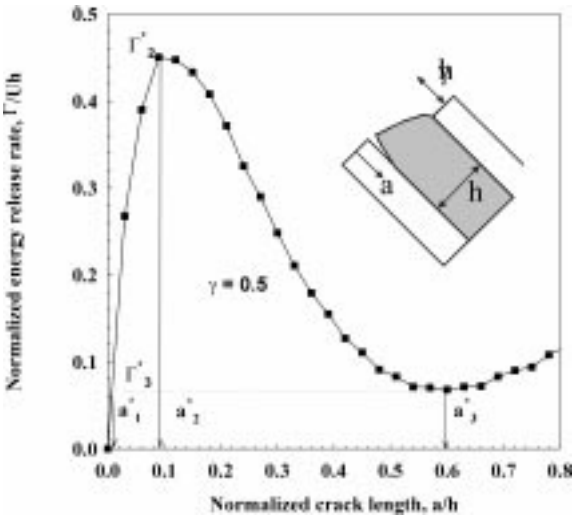

Fig. 4. Energy release rate as a function of crack length for strain $\gamma = 0.5$ (Jagota et al., 2000) showing different regimes of stable and unstable crack growth along the polymer/glass interface in a CSS test.

4. Long crack limit, $a_0^* > a_3^*$: flaw remains stationary until $\Gamma^* = \Gamma_0^*$, at which point the flaw would undergo unstable crack growth.

Fig. 4 shows the variation in energy release rate for a fixed strain, γ. The peak, Γ_2^*, is found to increase with shear strain. The minimum, Γ_3^*, has been found to be relatively insensitive to the applied shear strain.

The CSS experiment is chosen here as a vehicle for the demonstration of interfacial fracture modeling by cohesive elements as it contains a rich variety of behaviors enumerated above under finite strains. Crack growth in the stable range, $a_2^* < a_0^* < a_3^*$, has previously been analyzed by 2D quasi-static simulations (Jagota et al., 2000). Analysis of crack growth under other regimes and crack growth conditions require the use of techniques developed in this paper.

3. Computational model formulation

3.1. Bulk material constitutive behavior

An incompressible rate-independent hyperelastic model has been employed for the bulk polymer material. The deviatoric stress, σ', for the incompressible hyperelastic material is given as (Ogden, 1984)

$$\sigma' = 2DEV\left[\left(\frac{\partial W}{\partial I_1} + I_1\frac{\partial W}{\partial I_2}\right)B - \frac{\partial W}{\partial I_2}B^2\right], \tag{3}$$

where, $W(I_1, I_2) = \sum_{r+s=1}^{N} C_{rs}(I_1 - 3)^r(I_2 - 3)^s$ is the strain energy density functional; I_1 and I_2 are the first and second invariants of the right Cauchy–Green tensor, $\mathbf{B}$, defined as $\mathbf{B} = \mathbf{F}\mathbf{F}^{\mathbf{T}}$, $\mathbf{F}$ is the deformation gradient tensor, and, C_{rs} are material constants. For the special case, $N = 1$ and $C_{01} = 0$, the strain energy density functional simplifies to $W(I_1, I_2) = C_{10}(I_1 - 3)$, and represents a neo-Hookean hyperelastic material (Ogden, 1984). The deviatoric stress for the neo-Hookean material is then obtained as, $\sigma' = 2C_{10}(\mathbf{B} - 1/3I_1\mathbf{I})$, where $\mathbf{I}$ is the identity tensor, and $2C_{10} = G$, is the shear modulus of the neo-Hookean material. A simple shear deformation with shear strain, γ, is experienced by the polymer material in the CSS test

far from the free edge. For this case, the strain energy density is given as, $U = (1/2)G\gamma^2$, and the shear stress in the neo-Hookean material is given as, $\sigma_{12} = G\gamma$.

3.2. Cohesive zone model for interface

A typical eight-node cohesive element between two regular eight-node bulk finite elements is shown in Fig. 5. The cohesive element describes the deformation and failure of the interface between the two bulk finite elements. A phenomenological potential, $\phi(\Delta_n, \Delta_{t1}, \Delta_{t2})$, has been used to derive the tractions that resist relative motion across the cohesive surfaces as, $T_n = \partial\phi/\partial\Delta_n$, $T_{t1} = \partial\phi/\partial\Delta_{t1}$, $T_{t2} = \partial\phi/\partial\Delta_{t2}$, where T_n, T_{t1}, T_{t2} are the normal and two tangential tractions across the interface, respectively. The particular form employed in this study is a 3D generalization of the Xu and Needleman (1994) potential, augmented to offer resistance to inter-penetration of cohesive surfaces as

$$\phi(\Delta_n, \Delta_{t1}, \Delta_{t2}) = \Gamma_0 \left[1 - \left(1 + \frac{\Delta_n}{\delta_{\mathrm{cr}}} \right) \exp\left(-\frac{\Delta_n}{\delta_{\mathrm{cr}}} \right) \exp\left(-\frac{\Delta_{t1}^2 + \Delta_{t2}^2}{\delta_{\mathrm{cr}}^2} \right) \right] - [1 - H(\Delta_n)]\kappa\Delta_n^3, \tag{4}$$

where, Γ_0 is the fracture energy of interface, δ_{cr}, the characteristic critical opening displacement, $H(\Delta_n)$, the Heaviside step function, κ, the penalty parameter, and Γ_0, the work done in separating the interface by complete separation along either the normal or any one of the two tangential directions, respectively. The potential employed here is fully reversible and the work of failure of the interface is path and rate independent. The constitutive behavior described by the potential is completely specified by the two parameters, Γ_0 and δ_{cr}. The penalty term in Eq. (4) is activated only under compression ($\Delta_n < 0$) and does not affect the work of interfacial separation. The penalty parameter is estimated as, $\kappa = G/h_{\mathrm{e}}^2$, where G is the shear modulus of the bulk material, and h_{e} is the size of the cohesive element. G is estimated for an hyperelastic material as the average of the material coefficients C_{10} and C_{01}. This choice of parameter, κ, is large enough to suppress inter-penetration of cohesive surfaces without adversely affecting the numerical conditioning of the global set of equations. Fig. 6(a) shows a plot of the normal traction T_n across the cohesive surface as obtained by employing the penalty augmented potential of Eq. (4) along with the normal traction as obtained by the Xu and Needleman (1994) potential. Fig. 6(b) shows the variation of tangential traction T_{t1}. The variation of tangential traction T_{t2} is similar to that of tangential traction, T_{t1}. The maximum normal and tangential tractions are obtained as $\sigma_n^{\max} = \Gamma_0/e\delta_{\mathrm{cr}}$ and $\tau_{t1}^{\max} = \sqrt{2/e}\Gamma_0/\delta_{\mathrm{cr}}$ for the respective conditions, $\Delta_{t1} = \Delta_{t2} = 0$, and, $\Delta_n = \Delta_{t2} = 0$, where, $e = \exp(1)$, is the Euler number. The crack tip is defined as

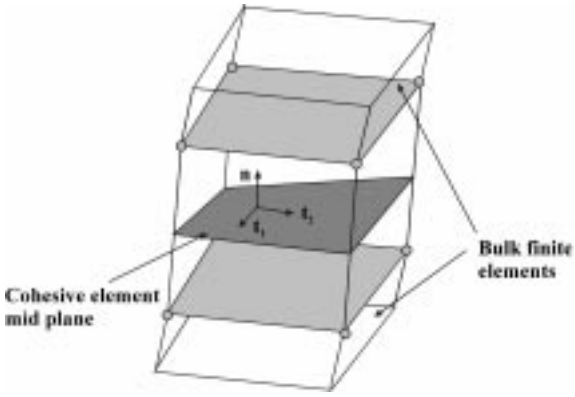

Fig. 5. Schematic drawing of an eight-node cohesive element between two 3D eight-node bulk elements and the local coordinate system used to define the tractions and openings.

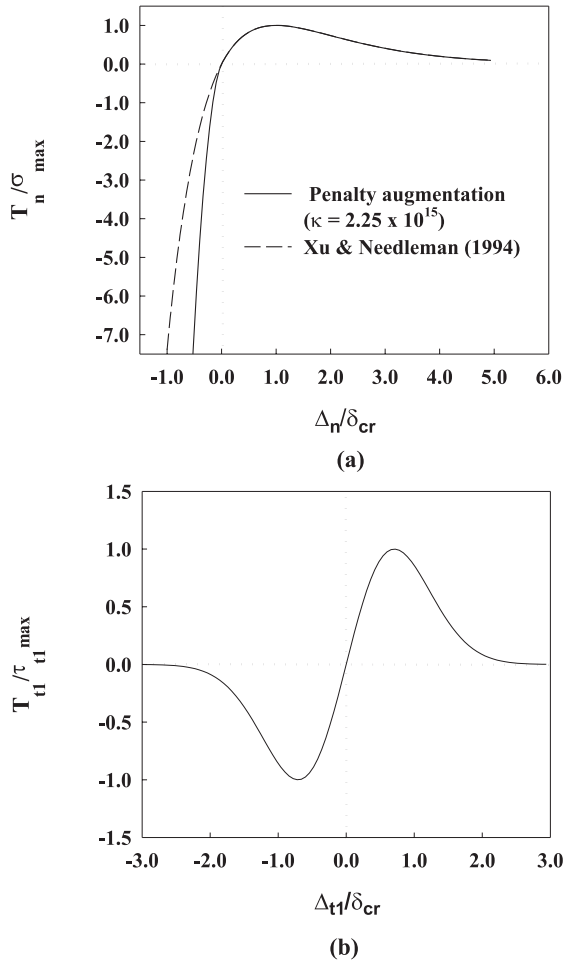

Fig. 6. (a) Normal tractions across cohesive surface with and without penalty augmentation in compression ($\Delta_n < 0$) for $\Delta_{t1} = \Delta_{t2} = 0$. (b) Tangential shear tractions across the cohesive surface for $\Delta_n = \Delta_{t2} = 0$.

the location along the interface where the combined openings (Δ_n, Δ_{t1}, Δ_{t2}) of the interface satisfy the relationship:

$$\left[1 - \left(1 + \frac{\Delta_n}{\delta_{\mathrm{cr}}}\right) \exp\left(-\frac{\Delta_n}{\delta_{\mathrm{cr}}}\right) \exp\left(-\frac{\Delta_{t1}^2 + \Delta_{t2}^2}{\delta_{\mathrm{cr}}^2}\right)\right] = 1 - \frac{2}{e}. \tag{5}$$

The work done in opening the cohesive zone as given by Eq. (4) under pure normal opening ($\Delta_{t1} = \Delta_{t2} = 0$) evaluates to, $(1 - 2/e)\Gamma_0$, for $\Delta_n = \delta_{\mathrm{cr}}$. The crack-tip location as identified by Eq. (5) ensures that the work done in opening the interface by a combination of openings (Δ_n, Δ_{t1}, Δ_{t2}) at the crack tip equals the work done under pure normal separation, $(1 - 2/e)\Gamma_0$. This definition of the crack-tip location is consistent with the potential defined in Eq. (4).

The actual cohesive law governing the failure process along the interface is often found to be rate dependent (Rahul-Kumar et al., 1999; Jagota et al., 2000). However, for the sake of demonstrating the ability of the cohesive element approach to model the variety of crack propagation behaviors observed in the CSS

experiment, it suffices for us to represent the bulk by continuum hyperelasticity, and the interface by a phenomenological rate-independent cohesive model. If one adopts this approximation, the fracture toughness includes contributions from the bulk viscous losses and fracture processes occurring in the crack-tip cohesive zone (Jagota et al., 2000). Such an analysis could be performed for various experimental strain rates shown in Fig. 3, where the hyperelastic constants C_{rs} are calibrated to fit an experimentally measured stress–strain curve at a specified strain rate.

3.3. Numerical formulation

Cohesive zone models have been implemented as cohesive finite elements within an implicit finite element framework. The principle of virtual work accounting for inertial effects and cohesive zone forces is given as

$$\int_V \rho \mathbf{a}\,\mathrm{d}V + \int_V \sigma : \delta\mathbf{d}\,\mathrm{d}V + \int_S \mathbf{T} : \delta\dot{\Delta}\frac{1}{J}\mathrm{d}S - \int_A F : \delta\mathbf{v}\,\mathrm{d}A = 0, \tag{6}$$

where ρ is the material density, $\mathbf{a}$, the acceleration, $\boldsymbol{\sigma}$, the Cauchy stress tensor; $\delta\mathbf{d}$, the virtual rate of deformation tensor; $\mathbf{T}$, the vector of cohesive tractions; $\delta\dot{\Delta}$, the vector of virtual velocity jumps across the cohesive surface, $\mathbf{F}$, the vector of externally applied tractions, $\delta\mathbf{v}$, the vector of the virtual velocity field, V, the current volume of the bulk material, S, the current internal surface area over which the cohesive forces are acting, A, the current external surface area over which the external tractions are applied, and J, the Jacobian of the transformation between the current deformed and original undeformed areas of the cohesive surfaces. The third term in Eq. (6) represents the contribution to virtual work due to cohesive zone tractions. A spatial discretization of this term and its first variation by using cohesive elements leads to the internal force vector, $\mathbf{F}_{\mathrm{c}}^{\mathrm{int}}$, and an approximate form of the tangent stiffness matrix, $\mathbf{K}_{\mathrm{c}}$, (Rahul-Kumar et al., 1999, 2000) as

$$\mathbf{F}_{\mathrm{c}}^{\mathrm{int}} = \int_S \mathbf{A}^T\mathbf{T}\frac{1}{J}\mathrm{d}S, \tag{7}$$

$$\mathbf{K}_{\mathrm{c}} \approx \int_S \mathbf{A}^T\mathbf{D}\mathbf{A}\frac{1}{J}\mathrm{d}S, \tag{8}$$

where $\mathbf{A}$ is a matrix of cohesive element shape functions that relates the cohesive element nodal velocities, $\bar{\mathbf{v}}$, to velocities of displacement jumps, $\dot{\Delta}$, within the cohesive element as

$$\dot{\Delta} = \mathbf{A}\bar{\mathbf{v}}, \tag{9}$$

where $\mathbf{D}$ is the cohesive element constitutive matrix that relates the incremental tractions, $\mathrm{d}\mathbf{T}$, to incremental displacement jumps, $\mathrm{d}\Delta$, within the cohesive element as

$$\mathrm{d}\mathbf{T} = \mathbf{D}\mathrm{d}\Delta, \tag{10}$$

where

$$\mathbf{D} = \begin{bmatrix} \frac{\partial T_n}{\partial \Delta_n} & \frac{\partial T_n}{\partial \Delta_{t1}} & \frac{\partial T_n}{\partial \Delta_{t2}} \\ \frac{\partial T_{t1}}{\partial \Delta_n} & \frac{\partial T_{t1}}{\partial \Delta_{t1}} & \frac{\partial T_{t1}}{\partial \Delta_{t2}} \\ \frac{\partial T_{t2}}{\partial \Delta_n} & \frac{\partial T_{t2}}{\partial \Delta_{t1}} & \frac{\partial T_{t2}}{\partial \Delta_{t2}} \end{bmatrix}. \tag{11}$$

The finite element spatial discretization of the virtual work expression in Eq. (6) at time $t + \Delta t$ is written as

$$\mathbf{M}\ddot{\mathbf{u}} + \mathbf{F}^{\mathrm{int}} - \mathbf{F}^{\mathrm{ext}} = \mathbf{0}, \tag{12}$$

where $\mathbf{M}$ is the mass matrix, $\ddot{\mathbf{u}}$ is the vector of nodal accelerations, and $\mathbf{F}^{\mathrm{int}}$ and $\mathbf{F}^{\mathrm{ext}}$ are the internal and external force vectors respectively, at time $t + \Delta t$. The internal force vector, $\mathbf{F}^{\mathrm{int}}$, has contributions from

cohesive element tractions, $\mathbf{F}_{\mathrm{c}}^{\mathrm{int}}$, and the bulk elements stresses, $\mathbf{F}_{\mathrm{b}}^{\mathrm{int}}$. The development of the cohesive element for the use in an implicit dynamic procedure within the nonlinear finite element analysis code ABAQUS® (1997) is performed by using the Hilber et al. (1978) implicit time integrator for the temporal discretization of Eq. (12). In this procedure, the equilibrium (12) at time $t+\Delta t$ is replaced by a weighted average of equilibrium statements at times t and $t+\Delta t$, respectively. The resulting virtual work equation is written as

$$\mathbf{r}(\alpha,\mathbf{u}_{t+\Delta t}) = \mathbf{M}\ddot{\mathbf{u}}_{t+\Delta t} + (\mathbf{1}+\alpha)(\mathbf{F}^{\mathrm{int}}_{t+\Delta t} - \mathbf{F}^{\mathrm{ext}}_{t+\Delta t}) - \alpha(\mathbf{F}^{\mathrm{int}}_{t} - \mathbf{F}^{\mathrm{ext}}_{t}) = \mathbf{0}, \tag{13}$$

where α defines the intermediate configuration between times t and $t+\Delta t$; and $\mathbf{u}_{t+\Delta t}$ is the vector of nodal displacements at time $t+\Delta t$. Eq. (13), along with the Newmark time integration formulae, forms the basis of the "predictor" step and the iterative Newton–Raphson "corrector" steps in solving for the configuration at time $t+\Delta t$ (Crisfield, 1997). The tangent matrix, $\overline{\mathbf{K}}^{i}_{t+\Delta t}$, and the residual, $\mathbf{r}^{i}(\alpha,\mathbf{u}^{i}_{t+\Delta t})$, used in the Newton–Raphson corrective iterations, i, are obtained by the linearization of the residual $\mathbf{r}(\alpha,\mathbf{u}_{t+\Delta t})$ given by Eq. (13) about the current iterative configuration, $\mathbf{u}^{i}_{t+\Delta t}$, as

$$\overline{\mathbf{K}}^{i}_{t+\Delta t} = (\mathbf{1}+\alpha)\mathbf{K}^{i}_{t+\Delta t} + (\mathbf{1}+\alpha)\delta\dot{\mathbf{u}}_{t+\Delta t}\mathbf{C}^{i}_{t+\Delta t} + \delta\ddot{\mathbf{u}}_{t+\Delta t}\mathbf{M}, \tag{14a}$$

$$\mathbf{r}^{i}(\alpha,\mathbf{u}^{i}_{t+\Delta t}) = \mathbf{M}\ddot{\mathbf{u}}^{i}_{t+\Delta t} + (\mathbf{1}+\alpha)(\mathbf{F}^{\mathrm{int},i}_{t+\Delta t} - \mathbf{F}^{\mathrm{ext,i}}_{t+\Delta t}) - \alpha(\mathbf{F}^{\mathrm{int},i}_{t} - \mathbf{F}^{\mathrm{ext,i}}_{t}), \tag{14b}$$

where $\mathbf{K}^{i}_{t+\Delta t}$ is the static tangent stiffness matrix, $\mathbf{C}^{i}_{t+\Delta t}$, the damping matrix, $\delta\dot{\mathbf{u}}_{t+\Delta t}$ and $\delta\ddot{\mathbf{u}}_{t+\Delta t}$ are the variations in nodal displacements and nodal accelerations, respectively. These are obtained from the Newmark integration formulae in terms of time the integration parameters and the time step size, Δt, (Crisfield, 1997). The damping matrix $\mathbf{C}^{i}_{t+\Delta t}$ is absent when the bulk polymer is modeled as an hyperelastic material. A cohesive element in which the constitutive calculations relate the tractions within the element to the openings across the element faces, the contributions to the damping and mass matrices as well as external loads are absent. The resulting tangent stiffness matrix and the residual vector for a cohesive element given in Eqs. (14a) and (14b) for the use in an implicit dynamic procedure simplify to

$$\overline{\mathbf{K}}^{i}_{t+\Delta t} = (\mathbf{1}+\alpha)\mathbf{K}^{i}_{t+\Delta t}, \tag{15a}$$

$$\mathbf{r}^{i}(\alpha,\mathbf{u}^{i}_{t+\Delta t}) = (\mathbf{1}+\alpha)\mathbf{F}^{\mathrm{int},i}_{t+\Delta t} - \alpha\mathbf{F}^{\mathrm{int},i}_{t}. \tag{15b}$$

The various quantities used in the evaluation of Eqs. (15a) and (15b) can be obtained by evaluating Eqs. (7) and (8) at times t and $t+\Delta t$, respectively. The constitutive calculations and the integrations of internal force vector and tangent stiffness matrix for these cohesive elements are performed on the mid-surface of the cohesive element (Fig. 5). This mid-surface is defined by the corresponding shape functions of the cohesive element and the coordinates that are an average of the current top and bottom cohesive element nodal coordinates. Eqs. (15a) and (15b) have been implemented as user elements in the nonlinear finite element code ABAQUS® (1997) for a family of 2D and 3D cohesive elements.

4. Dynamic crack growth in elastic double cantilever beam

Dynamic crack growth along an elastic double cantilever beam (DCB) has been studied to verify the implicit dynamic cohesive element procedures described. An elastic DCB specimen is opened at its free end at a specified constant velocity leading to the crack-tip propagating at a nonuniform velocity. The geometry of the DCB problem along with the loading conditions is shown in Fig. 7(a). An approximate analytical solution under small deformation assumptions using the Euler–Bernoulli beam theory was given by Bilek

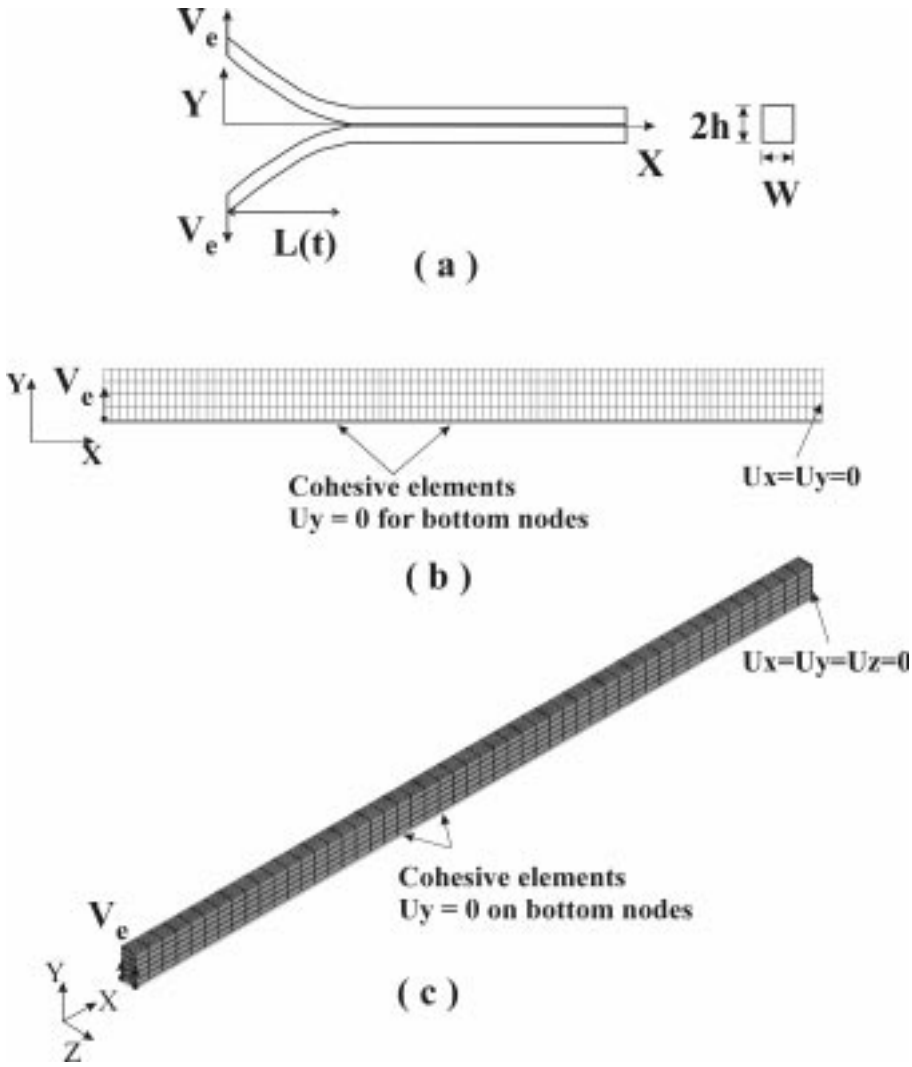

Fig. 7. (a) Schematic of the dynamic elastic DCB problem. (b) 2D Finite element discretization. (c) 3D Finite element discretization.

and Burns (1974). The solution predicts that the quantity $L^2(t)/t$ remains constant, where $L(t)$ is the crack length at time, t.

The DCB geometry has been modeled using (a) 2D, four-node plane stress elements with four-node cohesive elements, and, (b) 3D, eight-node brick elements with eight-node cohesive elements. Based on symmetry considerations, only one arm of the DCB is modeled here. Finite element meshes along with the kinematic and symmetry boundary conditions are shown in Figs. 7(b) and (c) for the 2D and 3D analysis, respectively. The 3D mesh has five elements through the depth and thickness of the beam. Cohesive elements are placed for the entire length of the DCB along the plane of symmetry, $y = 0$. The nodes on the top face of the cohesive elements are constrained to have the same displacement in the x direction as the corresponding nodes on the bottom face. The DCB geometry, material, and cohesive element parameters employed in the analysis are $h = 0.25$ m, $w = 0.125$ m for the 2D plane stress and 3D models, $V_e = 31.62$ m/sec, $E = 100$ GPa, $\rho = 2000$ kg/m^3, $\Gamma_0 = 10^6$ N/m, $\delta_{cr} = 0.01$ m. The crack length, $L(t)$, is defined by Eq. (5).

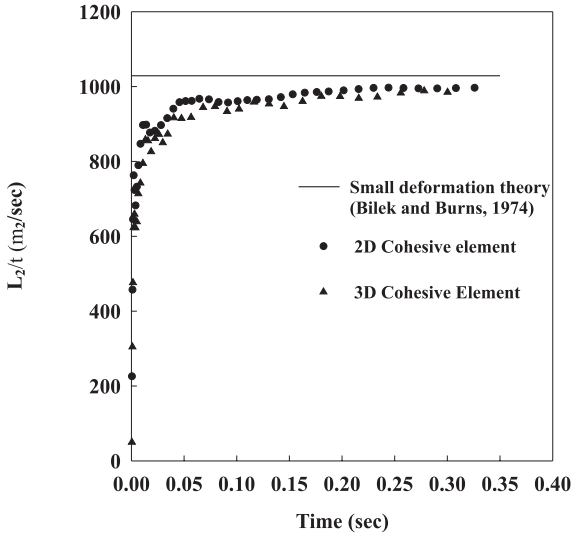

Fig. 8. Dynamic crack growth in a 2D and 3D elastic DCB using 2D four-node and 3D eight-node cohesive elements.

A plot of the quantity, $L^2(t)/t$, versus time, t, as obtained from the 2D and 3D simulations has been compared with the respective approximate analytical results of Bilek and Burns (1974) in Fig. 8. The numerical solutions converge to the constant analytical solutions as $L(t)$ increases with time, t, thus validating the cohesive element implementation. The small oscillations in the computed values of $L^2(t)/t$, are an indication of transient vibrations in the beams during dynamic crack growth as analyzed by Williams (1999).

5. 2D analysis of crack propagation in compressive shear strength test

The crack growth behaviors for different sizes of the pre-flaw, a_0^*, along the glass/polymer interface have been simulated using cohesive elements. These simulations verify the stable and unstable crack growth regimes described in Section 4 and demonstrate the ability of cohesive element technique to model various crack growth behaviors in interfacial failures.

A 2D plane strain model of the CSS test specimen with polymer thickness, $h = 0.76$ mm, has been used in this study. A representative finite element discretization of the model, employing four-node hybrid elements for the polymer and regular four-node displacement based elements for glass is shown in Fig. 9. A layer of four-node cohesive elements is placed along the interface between the polymer and glass. The mesh has a starter region adjacent to the free edge of size $8h$ along the length with cohesive elements of size $0.05h$. The loading consists of specifying displacements, $u_x = 0$ and $u_y = \gamma h/\sqrt{2}$, for the nodes on the top surface of bulk polymer elements. The boundary conditions for the nodes on the bottom surface of the glass elements are specified as $T_x = 0$, and $u_y = 0$. The polymer material has been modeled as a neo-Hookean hyperelastic material with material constant, $C_{10} = (1/2)G = 1.66 \times 10^5$ Pa, and density, $\rho = 1070$ kg/m^3. Glass has been modeled as a rigid substrate.

A quasi-static simulation of the CSS test has been performed using discretizations similar to the one described above employing cohesive elements of size $0.05h$ and smaller to investigate the mesh sensitivity of the computed results. The simulations have been performed for an applied shear strain, $\gamma = 1.1$. A pre-flaw of size $a_0 = 0.25h$ in the intermediate crack regime has been placed along the interface to avoid the initial

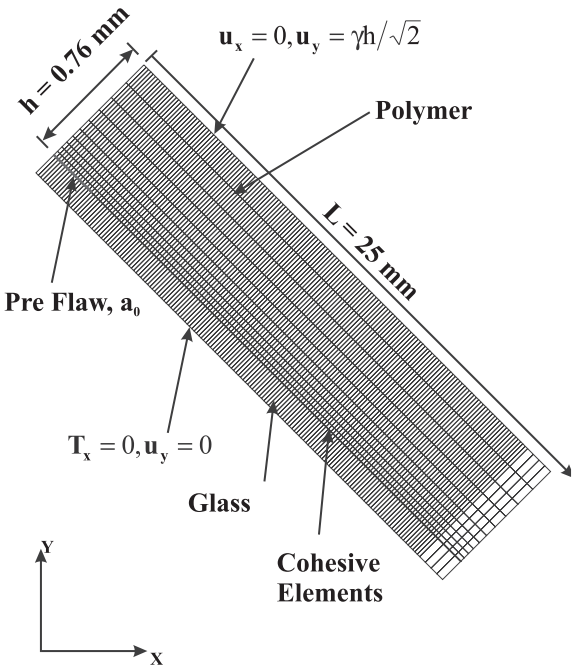

Fig. 9. Representative finite element discretization used in the CSS simulations.

instability in crack growth for smaller pre-flaw sizes. The cohesive zone model parameters employed are $\Gamma_0 = 4.95$ N/m, and $\delta_{cr} = 10$ μm. The crack length, a, is defined by Eq. (5). The computed normalized crack length, a^*, as function of applied strain, γ, for the various discretizations employed revealed negligible mesh sensitivity. The normalized fracture energy, Γ_0, as a function of the normalized crack length, a^*, have also been compared and the results have been found to be insensitive to the discretization.

The performance of the cohesive element method based on penalty formulation of Eq. (4) for avoiding the inter-penetration of the cohesive surfaces under compression has been compared against the Lagrange multiplier based technique for enforcing contact constraints in ABAQUS® (1997) program. The differences in the computed results for the normalized fracture energy, Γ_0, as a function of the normalized crack length, a^*, have been found to be insignificant for the two methods used to enforce the contact constraints.

5.1. Intermediate crack analysis ($a_2^* < a_0^* < a_3^*$)

As discussed in Section 2, a pre-flaw in the intermediate crack regime, $a_2^* < a_0^* < a_3^*$, is predicted to grow stably upto a critical shear strain, γ^*, and unstably thereafter. A family of energy release rate curves for various levels of applied shear strain γ were obtained by Jagota et al. (2000) and have been plotted as dashed line curves in Fig. 10. The minimum, Γ_3^*, in energy release rate curves has been found to be relatively insensitive to the applied shear strain, γ. An empirical linear fit for the variation in, Γ_3^*, as a function of, γ, has been developed by Jagota et al. (2000) and reported as, $\Gamma_3^* = 0.0717 + 0.00574\gamma$. At the instant of instability, $\Gamma_3^* = \Gamma_0^*$, and, $U = (1/2)G\gamma^{*2}$, for neo-Hookean hyperelasticity. The relationship between the strength of the interface, Γ_0, and the critical strain to instability, γ^*, is then obtained as

$$\Gamma_0 = \frac{1}{2}Gh(0.0717 + 0.00574\gamma^*)\gamma^{*2}. \tag{16}$$

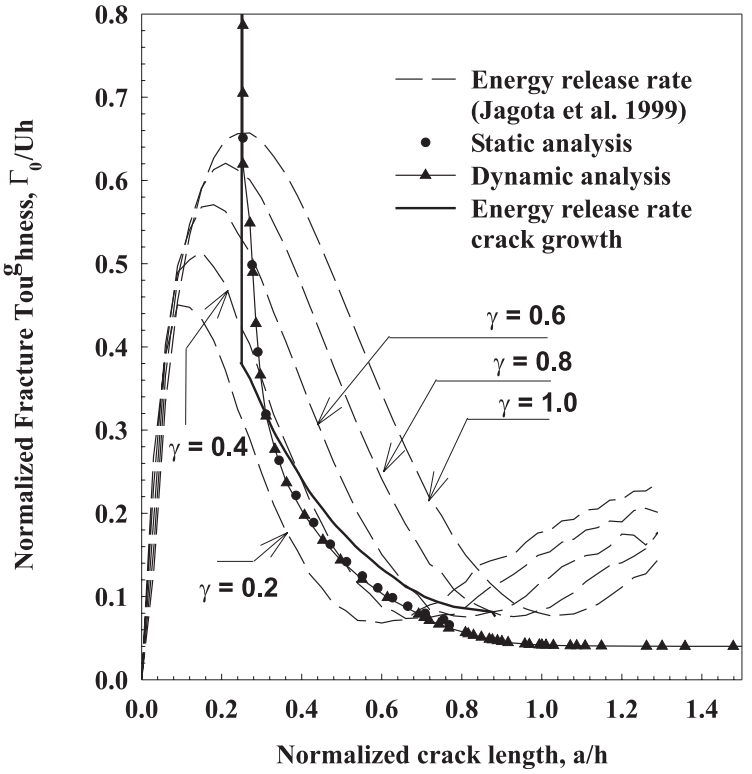

Fig. 10. Comparison of normalized fracture energy predicted by static analysis and dynamic analysis employing cohesive elements with energy release rate crack growth prediction based on Eq. (1). The dashed line curves are energy release rate curves for various levels of applied shear strain γ as developed by Jagota et al. (2000).

For an interface characterized by, $\Gamma_0 = 4.95$ N/m, the critical shear strain at instability, γ^*, and the normalized fracture energy at instability, Γ_0^*, are obtained as 0.72 and 7.58×10^{-2}, respectively. For an interface of strength, Γ_0, the equilibrium crack location a_e^* for various levels of applied shear strain γ based on an energy release rate analysis is given by Eq. (1). The crack growth obtained by solving Eq. (1) for $\Gamma_0 = 4.95$ N/m for various levels of applied shear strain γ with an initial pre-flaw of size $0.25h$ has been plotted as the dark solid line curve in Fig. 10. The crack growth so predicted is referred to as the, "energy release rate crack growth".

In a CSS test simulation with cohesive elements characterized by, $\Gamma_0 = 4.95$ N/m and $\delta_{cr} = 10.0$ μm, the crack growth from an initial pre-flaw of size $0.25h$ in the intermediate crack regime is expected to be stable until the applied shear strain reaches 0.72. A quasi-static simulation of the CSS test has been performed using the discretization shown in Fig. 9. A plot of normalized fracture energy, Γ_0^*, as a function of the normalized crack length, a^*, as obtained by from the quasi-static simulation has been plotted in Fig. 10. The crack growth predicted by cohesive element modeling agrees well with the energy release rate crack growth prediction. At $\Gamma_0^* = \Gamma_3^*$, crack growth is unstable and cannot be modeled by the static solution procedure. The quasi-static simulation terminates here due to numerical instabilities resulting from unstable crack growth. The instant of instability in terms of applied shear strain defined through Γ_0^*, obtained using quasi-static simulation employing cohesive elements is in agreement with the 2D plane strain energy release rate analysis. However, as seen from Fig. 10 there is a small discrepancy in terms of the normalized crack lengths when the crack growth goes unstable.

The dynamic analysis of the CSS test employing the discretization shown in Fig. 9 with cohesive elements characterized by the above stated parameters has been performed. The predicted normalized fracture energy, Γ_0^*, as a function of normalized crack length, a^*, has been plotted in Fig. 10. Predictions from quasi-static and dynamic simulations are in good agreement over the solution history. The dynamic analysis simulation proceeds beyond the instability limit predicted by Eq. (16) based on the energy release rate analysis. The crack eventually goes unstable when, $\Gamma_0^* = 4.0 \times 10^{-2}$, as evident by the zero slope of the dynamic analysis curve. The difference between the values of Γ_0^* at instability as predicted by a quasi-static energy release rate analysis versus the dynamic analysis is attributed to the finite rate of loading in the dynamic simulation. A normalized measure of the shear strain rate in the dynamic simulation is, $\dot{\gamma}h/c$, where, $\dot{\gamma}$ is the applied shear strain rate, and, $c = \sqrt{G/\rho}$, the shear wave speed in the polymer material. The value, $\Gamma_0^* = 4.0 \times 10^{-2}$, corresponds to a normalized rate of straining of, $\dot{\gamma}h/c = 6.4 \times 10^{-3}$. It has been observed that as the applied shear strain rate is decreased, Γ_0^* at instability increases, and approaches the limit 7.58×10^{-2} predicted by quasi-static energy release rate analysis.

Plots of the deformation sequence and the location of the crack tip from the dynamic analysis simulation are shown in Fig. 11(a)–(e). Fig. 11(a) and (b) show the deformation and crack openings prior to instability.

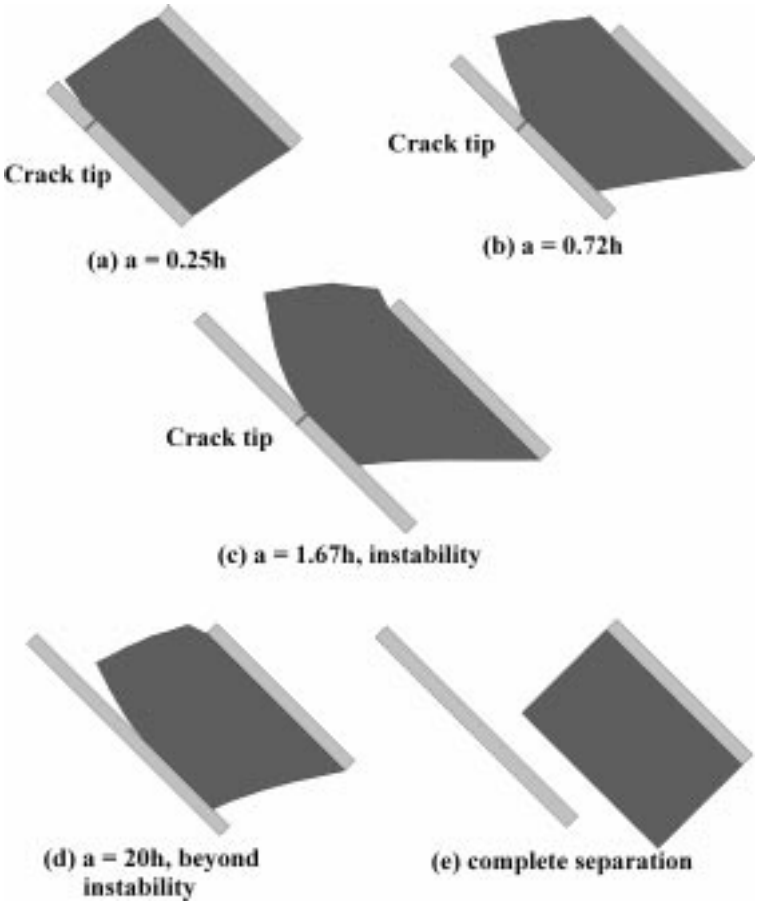

Fig. 11. (a–e) Deformation sequences for a CSS test simulation with an initial pre-flaw size in the intermediate crack length regime.

Fig. 11(c) shows the deformation at the instant when the crack goes unstable. Fig. 11(d) shows the deformation after the instability when considerable sliding occurs along the interface. The polymer starts to unload and begins to recover its original configuration. Fig. 11(e) shows complete separation of the polymer and glass surfaces. The polymer unloads and completely recovers its original configuration. This sequence of deformations is in good agreement with the experimental deformations shown in Fig. 2(a) and (b).

5.2. Short crack analysis ($a_1^* < a_0^* < a_2^*$)

In this regime of pre-flaw sizes crack growth in a CSS test is predicted to "pop-in" at a certain critical strain level and grow dynamically to a crack length in the intermediate crack length regime. Subsequently, upon continued straining, the crack undergoes stable crack growth and eventually goes unstable. For an interface characterized by, $\Gamma_0 = 4.95$ N/m, the energy release rate crack growth from a pre-flaw in the short crack regime of size, $a_0 = 0.05h$, as obtained by solving Eq. (1) has been plotted as the dark solid line in Fig. 12. Based on the plot, it is observed that the pre-flaw would pop-in at a normalized fracture energy, $\Gamma_0^* = 0.29$, to a normalized crack length of $a^* = 0.33$. This dynamic pop-in of the crack is followed by stable crack growth and final instability at a normalized fracture energy, $\Gamma_0^* = 7.58 \times 10^{-2}$, corresponding to a critical shear strain, $\gamma^* = 0.72$.

A dynamic analysis has been performed to study crack growth from a pre-flaw of size, $a_0 = 0.05h$, in the short crack regime. The cohesive zone parameters employed in the simulation are: $\Gamma_0 = 4.95$ N/m,

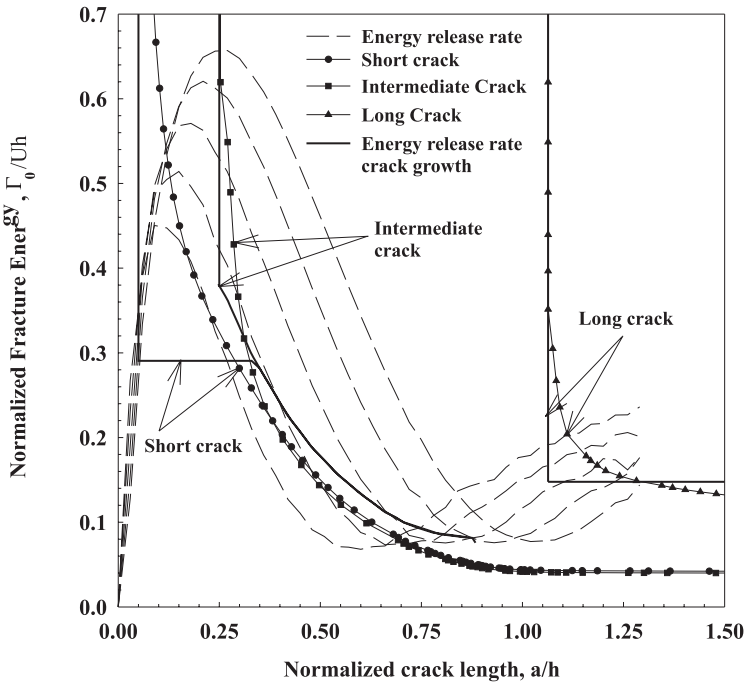

Fig. 12. Normalized fracture energy as a function of normalized crack length as obtained by dynamic analysis employing cohesive elements for simulating crack growth from different initial pre-flaw sizes in a CSS test with interface fracture energy $\Gamma_0 = 4.95$ N/m. The dark solid line curves are the corresponding energy release rate crack growth predictions based on Eq. (1).

$\delta_{cr} = 10.0$ μm. The predicted normalized fracture energy, Γ_0^*, as obtained from this simulation has been plotted in Fig. 12. The crack growth behavior predicted by cohesive element technique does not reveal such a sharp "pop-in" response. It is observed that crack growth continues under stable conditions and the interface fails at normalized fracture energy, $\Gamma_0^* = 4.0 \times 10^{-2}$. The energy release rate approach is based on the idealization of a "mathematically" sharp crack tip. The size of the cohesive zone, L, at the instant when crack growth initiates from the pre-flaw has been computed in the present analysis to be $0.37h$. The cohesive zone tip is identified as the location along the interface where the combined openings, Δ_n, Δ_{t1}, and $\Delta_{t2} = 0$, evaluate the potential in Eq. (4) to one percent of the work required for pure normal separation, $(1 - 2/e)\Gamma_0$. The distance between the crack tip as identified by Eq. (5) and the cohesive zone tip is reported as the cohesive zone size, L. The presence of such a large cohesive zone in the glass/polymer interface during crack initiation smears the crack-tip zone and the crack tip cannot be characterized as "mathematically sharp". This results in stable crack growth without the "pop-in". The results for the simulation with a pre-flaw in the intermediate crack size regime from earlier analysis in Section 5.1 have also been plotted in Fig. 12. The corresponding energy release rate crack growth prediction has been plotted as the dark solid line. As expected the normalized fracture energy Γ_0^* at final instability for the short-crack and intermediate crack length simulations are in agreement.

The effect of cohesive zone size, L, varied via the δ_{cr} parameter, on the simulated "pop-in" response has been investigated. The evolution of the normalized cohesive zone size, L/h, as a function of the normalized crack length, a^*, for different values of δ_{cr} ranging between 2.5 and 20 μm have been plotted in Fig. 13. This range of δ_{cr} has been found suitable for modeling the cohesive zone in the experiments (Jagota et al., 2000).

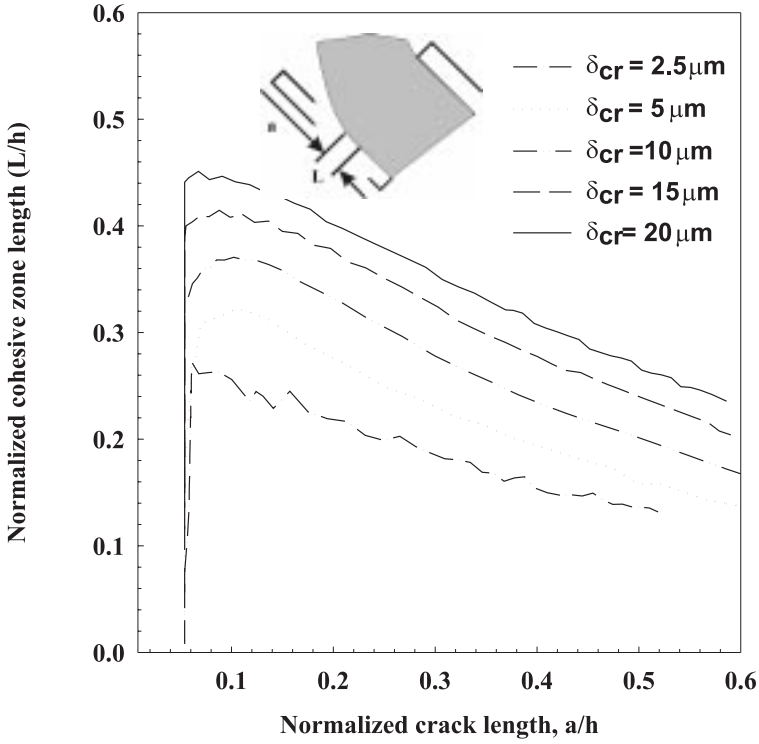

Fig. 13. Evolution of normalized cohesive zone size for different values of the δ_{cr} parameter employed during the CSS test simulation with a pre-flaw in the short crack regime.

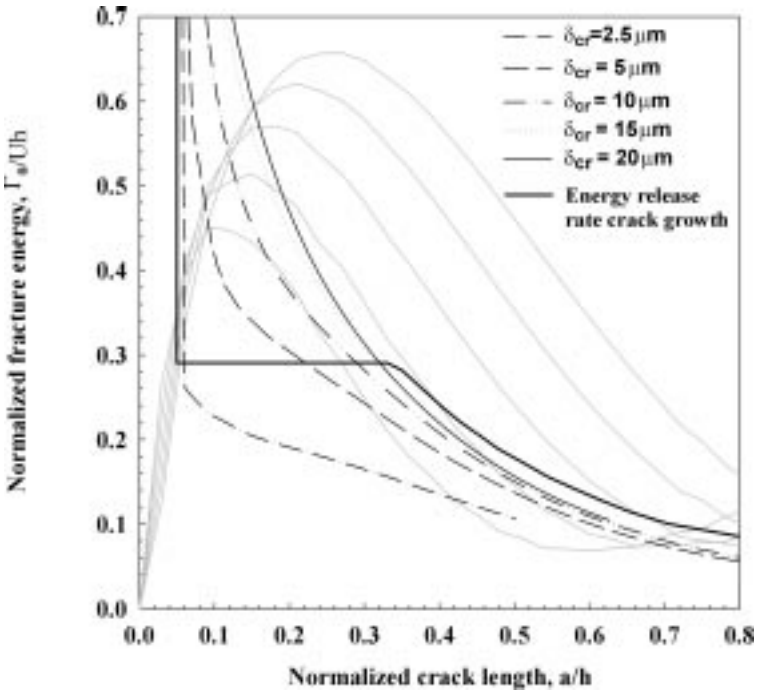

Fig. 14. "Pop-in" response from a pre-flaw in the short crack regime in terms of normalized fracture energy and normalized crack length for different values of the parameter δ_{cr}.

The cohesive zone sizes start out in the range 0.27–0.46h at the instant when crack growth initiates from the pre-flaw. It decreases in size for a given δ_{cr} as the crack grows. The initiation of crack growth from the pre-flaw in the glass/polymer interface is thus characterized by the presence of relatively large cohesive zone sizes precluding the existence of "pop-in". The predicted crack growth responses in terms of normalized fracture energy, Γ_0^*, for various values of δ_{cr} values have been plotted in Fig. 14. It is observed that as δ_{cr} decreases the crack growth from the pre-flaw initiates at progressively smaller values of Γ_0^*. For $\delta_{cr} = 2.5$ μm, crack growth from the pre-flaw does not initiate till the normalized fracture toughness of the interface, Γ_0^*, reaches the initial rising part of the energy release rate curve and agrees well the energy release rate based response for crack pop-in. At this instant, the crack growth occurs in a mild pop-in-like fashion as evident by the relatively large increase in the crack length for a small change in the normalized fracture energy, Γ_0^*. Fig. 15 shows a plot of rate of change in crack length as a function of the applied shear strain, γ. Crack initiation from the pre-flaw is progressively delayed with decreasing value of δ_{cr}. From Fig. 15, it is observed that for the case of $\delta_{cr} = 2.5$ μm crack initiation from the pre-flaw is completely suppressed till the applied shear strain attains a critical value of 0.39 compared to shear strain at pop-in of 0.37 as predicted by the energy release rate approach. The sudden rise in the rate of change in crack length leads to rapid growth which proceeds till the crack length reaches a length in the intermediate crack length regime.

The results of the present analyses indicate that the sizes of the cohesive zones in glass/polymer interface are comparable to the thickness of the polymer material during crack initiation from these pre-flaws. Prior to any crack growth, under increasing applied shear strain, the crack-tip cohesive zone first develops ahead of the pre-flaw, i.e., the crack tip at the pre-flaw encounters an 'R-curve'. The presence of such a large cohesive zone along the glass/polymer interface and the increasing resistance to crack growth leads to stable

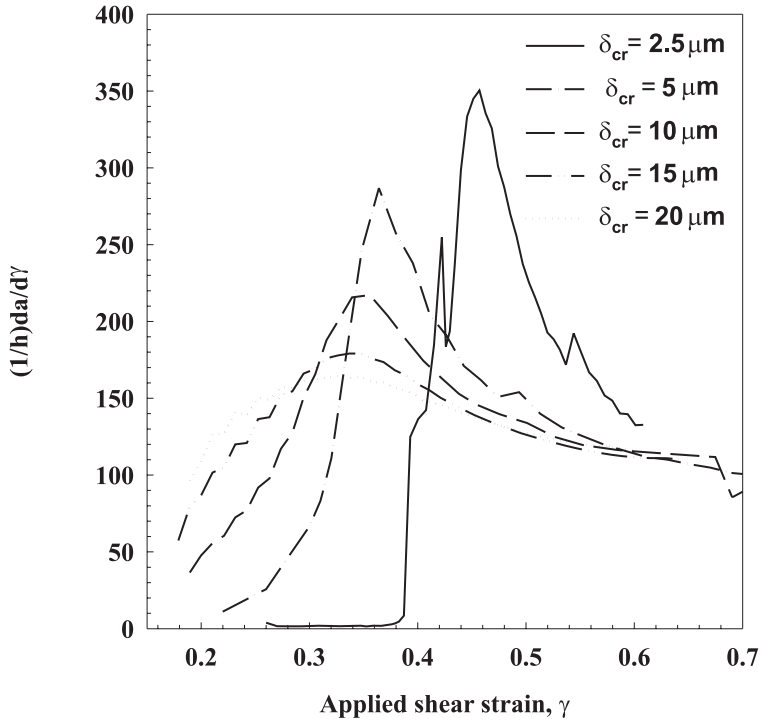

Fig.15. "Pop-in" response in terms of normalized rate of change of crack length, $(1/h)\,\mathrm{d}a/\mathrm{d}\gamma$, with applied shear strain, γ, for different values of the parameter δ_{cr}.

crack nucleation at the free edge from existing pre-flaws and subsequent stable growth as observed in the CSS experiments, and different from prediction based on an energy release rate analysis.

5.3. Long crack analysis ($a_0^* > a_3^*$)

For pre-flaws, $a_0^* > a_3^*$, energy release rate analysis predicts the crack growth to be unstable when the applied shear strain reaches a critical value. No crack growth is expected for shear strains below the critical value. For an interface characterized by, $\Gamma_0 = 4.95$ N/m, the energy release rate crack growth from a pre-flaw in the long crack regime of size, $a_0 = 1.25h$, as obtained by solving Eq. (1) has been plotted as the dark solid line in Fig. 12. It is observed that there is no crack growth from the pre-flaw until the normalized fracture energy, $\Gamma_0^* = 0.15$, corresponding to a shear strain of, $\gamma = 0.51$. Subsequently, the crack goes unstable.

A dynamic simulation of the CSS test has been performed with a pre-flaw size of $a_0 = 1.25h$, with cohesive zone model parameters, $\Gamma_0 = 4.95$ N/m and $\delta_{\mathrm{cr}} = 10$ μm. The predicted normalized fracture energy, Γ_0^*, as function of the normalized crack length, a^*, has been plotted in Fig. 12. It is observed that crack growth does not initiate till the strain reaches a critical value. This is evident from the vertical drop in the response for decreasing normalized fracture toughness Γ_0^* corresponding to increasing shear strain, γ. For the cohesive zone model properties employed here, at a normalized fracture energy, $\Gamma_0^* = 0.1$, corresponding to a critical shear strain of, $\gamma = 0.63$, the crack growth for the pre-flaw goes unstable. The energy release rate analysis predicts unstable crack growth for, $\Gamma_0^* = 0.15$. The difference, as explained before, arises due to the finite shear strain rate, $\dot{\gamma}h/c = 6.4 \times 10^{-3}$, employed in the dynamic simulation.

6. 3D analysis of crack propagation in compressive shear strain test

A 3D analysis of the CSS test has been performed by employing 3D cohesive elements and an hyperelastic material model for the polymer. The 3D finite element discretization employed in the study is shown in Fig. 16. The dimensions of the 3D CSS test specimen used in the 3D numerical study are polymer thickness, $h = 0.76$ mm, length= 25 mm, and width= 4.56 mm ($6h$). Based on symmetry about the x–y plane, one half of width ($3h$) is modeled in the z direction. The polymer is modeled by using eight-node hybrid brick elements, and glass is modeled using regular displacement based eight-node brick elements. A layer of 3D eight-node cohesive elements is placed along the interface between the polymer and glass. The size of cohesive elements in the fine discretized region in Fig. 16 at the free edge, $z = 3h$, are of dimension $0.047h$ along the length and $0.094h$ along the width. The 3D discretization consists of 48,900 degrees of freedom. The boundary conditions for the nodes on the bottom surface of the glass elements are specified as, $T_x = 0$, $u_y = 0$, $T_z = 0$. The nodes on the symmetry face, $z = 0$, have, $u_z = 0$. The loading consists of specifying displacements, $u_x = 0$, $u_y = \gamma h/\sqrt{2}$, and $u_z = 0$, for the nodes on the top surface of bulk polymer elements, where γ is the equivalent shear strain in the polymer material. The polymer material has been modeled as a neo-Hookean hyperelastic material with material constant, $C_{10} = (1/2)G = 1.66 \times 10^5$ Pa. Glass has been modeled as a rigid substrate. The cohesive zone parameters are: $\Gamma_0 = 4.95$ N/m, and $\delta_{cr} = 10.0$ μm. An implicit-dynamic analysis has been performed to simulate the stable and unstable crack growth along the interface.

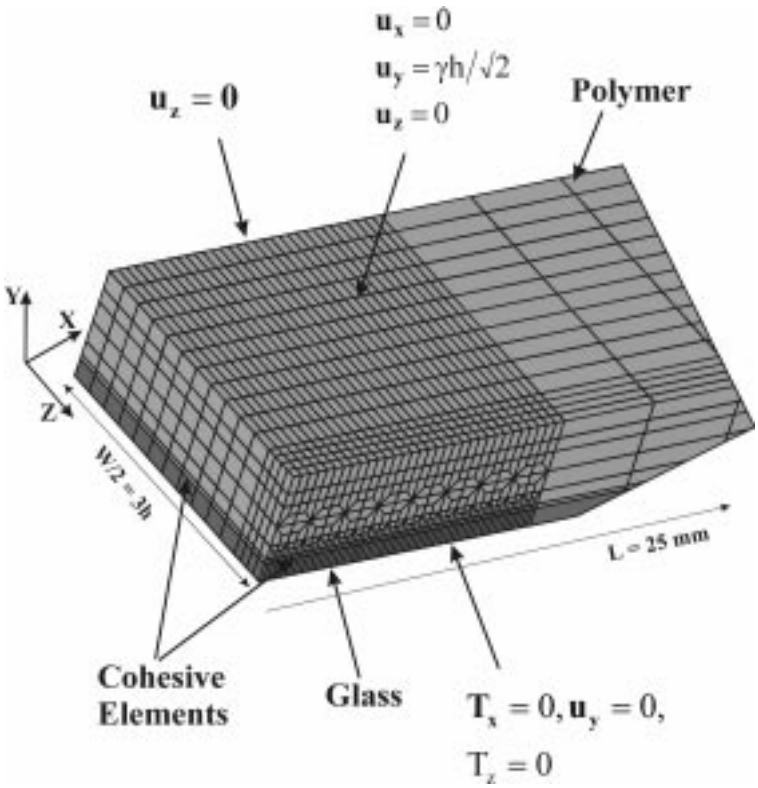

Fig. 16. Finite element discretization of one-half of the CSS test specimen employed in the 3D simulation of the test.

The dynamic simulation has been performed for an initial pre-flaw of size $a_0 = 0.25h$, which lies in the intermediate crack regime. The evolution of crack front in the simulation along the interface for different levels of applied shear strain has been plotted in Fig. 17. For a given level of applied shear strain the crack front contour is obtained by joining points along the interface where the openings (Δ_n, Δ_{t1}, Δ_{t2}) satisfy the relationship (5). Failure initiates ahead of the pre-flaw at an applied shear strain of, $\gamma = 0.183$, and is localized in the region near the free edge. At an applied shear strain, $\gamma = 0.281$, a tunneling of the failure located at the edges occurs and the crack front occupies the entire width of the specimen. The crack front at this instant is relatively straight. For progressively increasing shear strain, the crack front moves along the interface by developing a finite curvature at the free edge. About a distance of $2h$ from the free edge the crack front becomes straight implying plane strain conditions. Moving from the interior towards the free edge, crack length increases, attains a maximum value, and decreases near the free edge. At an applied shear strain of $\gamma = 0.704$ instabilities occur in the 3D simulation due to a local "pop-through" of the crack front at the free edge. At an applied strain of $\gamma = 0.782$, the crack front at the free edge undergoes a complete pop-through and the crack front curvature changes sign. At this instant, the crack is longer at the free edge when compared to interior of the specimen. Similar crack front profiles have been observed experimentally for crack growth along glass/epoxy interface (Swadener and Liechti, 1998). Finally, unstable crack growth and failure of the interface occurs at a strain of $\gamma = 0.868$.

Contour plots of the openings, Δ_n, Δ_{t1}, Δ_{t2}, along the interface for applied shear strain, $\gamma = 0.81$, are shown in Fig. 18. The tangential openings Δ_{t1}, Δ_{t2} are localized near the free edge and vanish within the distance, $2h$. At the free edge, they are of magnitude comparable to Δ_n. Nakamura (1991) conducted 3D

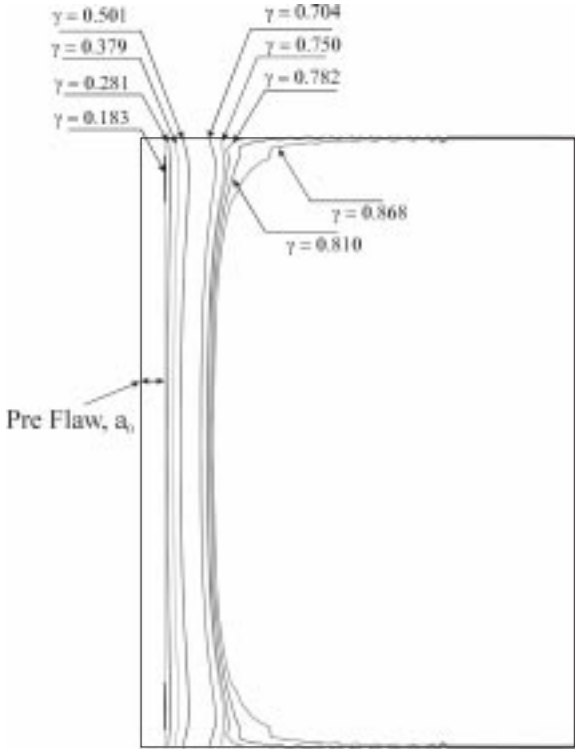

Fig.17. Evolution of failure and crack front along the interface in CSS test specimen for polymer modeled as Neo-Hookean hyperelastic material.

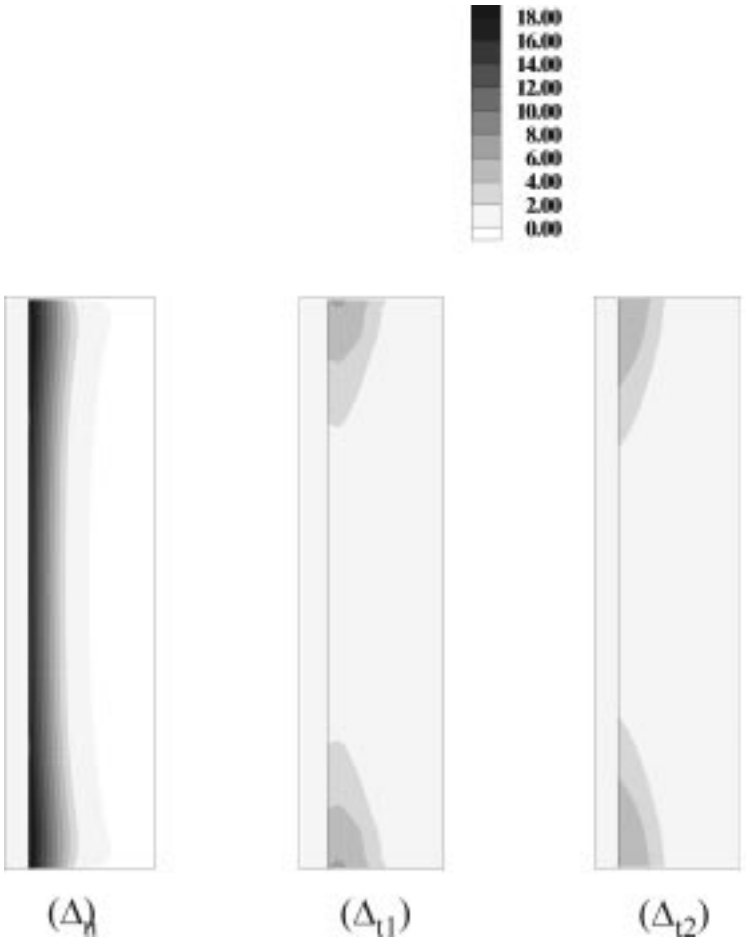

Fig. 18. Contours of openings, Δ_n, Δ_{t1}, Δ_{t2}, ahead of the pre-flaw along the glass/polymer interface at failure strain, $\gamma = 0.81$.

finite element analysis for an interfacial crack between elastic material and rigid substrate and finds similar results for the openings at the free edge. The local energy release rate is considerably larger at the free edge than at the interior. This leads to the curvature of the crack front at the free edge.

The predicted normalized fracture energy, Γ_0^*, as a function of the normalized crack length, a^*, has been plotted in Fig. 19. The crack length, a, for the 3D simulation is defined as the location along the free edge, $z = 3h$, where the openings (Δ_n, Δ_{t1}, Δ_{t2}) satisfy the relationship (5). For comparison purposes, the results of the 2D plane strain dynamic simulation from Section 5.1 employing same parameters for the polymer and the cohesive zone have also been plotted in Fig. 19. The 3D simulation predicts unstable crack growth at a normalized fracture toughness, $\Gamma_0^* = 5.2 \times 10^{-2}$ compared to the value of $\Gamma_0^* = 4.0 \times 10^{-2}$ as predicted by 2D plane strain analysis.

7. Conclusions

A family of cohesive elements for the use in static and implicit dynamic finite element procedures has been developed. When introduced between regular continuum elements, these provide a powerful tool for

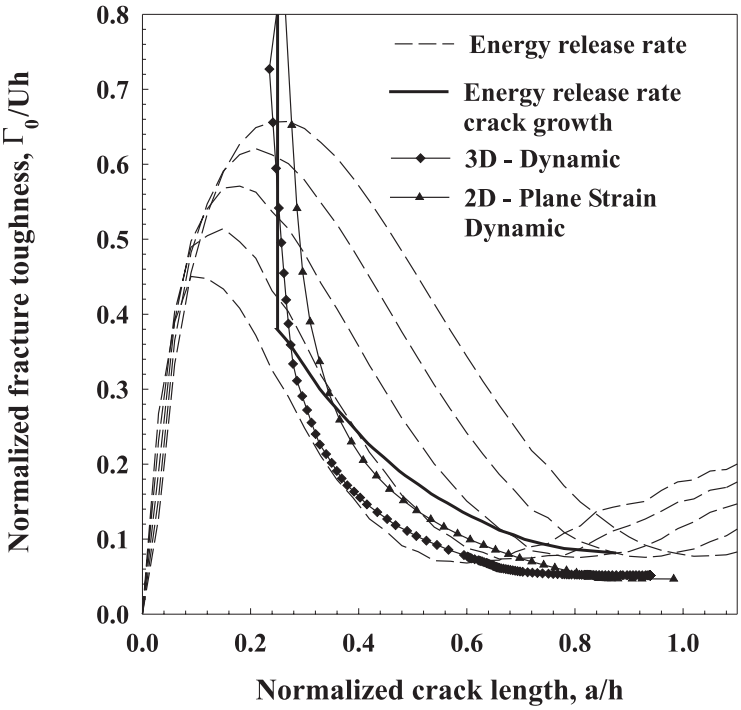

Fig. 19. Normalized fracture energies as obtained by 2D plane strain and 3D dynamic simulations of a CSS test with $\Gamma_0 = 4.95$ N/m. The crack growth based on 2D plane strain energy release rate analysis as given by Eq. (1) is shown as the dark solid line curve.

the study of fracture in situations not easily amenable to analysis using conventional techniques of fracture mechanics. The cohesive element family has been developed for the use with standard implicit finite element methods. The ability of the technique to model two- and three-dimensional, dynamic and quasi-static crack growth has been demonstrated by analyzing interfacial failures in a CSS test for polymer/substrate adhesion.

The following three types of crack growth are predicted in this experiment based on energy release rate analysis. Long cracks remain stationary until critical strain, and then propagate unstably. Pre-cracks with an intermediate length remain stationary until a critical applied strain, then grow stably, and eventually propagate unstably at a critical value of applied strain. Small cracks are predicted to remain stationary until a critical strain, to pop-in dynamically, grow stably, and eventually to propagate unstably at the same critical value of applied strain as intermediate length pre-cracks. Crack growth with pre-cracks in these three ranges of lengths have been analyzed using an hyperelastic constitutive equation for the bulk polymer and cohesive elements to represent the polymer/substrate interface. The dynamic cohesive element technique is able to capture all types of predicted behavior. For cracks in the intermediate length regime, dynamic and static results are in good agreement. Differences in critical strain at ultimate interfacial failure between the two result from finite rate of loading in the dynamic analysis.

For short cracks, the cohesive zone sizes are substantial in size compared to the polymer thickness, for physically realistic values of critical cohesive opening size, δ_{cr}. Due to the presence of such large cohesive zone at the crack tip, crack growth from such short cracks experiences a 'R-curve' with increasing value of applied shear strain. The finite size of cohesive zone and the 'R-curve' like resistance experienced by the crack tip causes the dynamic pop-in as predicted by quasi-static energy release rate analysis to be stabilized

in the cohesive element simulations. As δ_{cr} is reduced, the crack propagation behavior resembles a dynamic crack pop-in.

Free edge effects in the CSS experiment have been studied by three-dimensional analyses. Significant mixed mode deformation has been found up to a distance of twice the polymer thickness from the free edge, as measured by relative tangential displacements across the cohesive zone. The associated increase in local energy release rate near free edge causes crack length to be longer there. The 3D implicit-dynamic simulation is able to capture the stable and unstable parts of the crack growth in the CSS test. The simulation also reveals that the crack front undergoes a local "pop-through" at the free edge accompanied by local instabilities.

These examples demonstrate the ability of the cohesive element technique to model interfacial crack growth under a variety of conditions. The technique has the ability to model crack initiation and growth under complex conditions such as finite strains, inelastic material behavior, static and dynamic growth conditions. Crack initiation and growth criteria are specified within the cohesive zone model itself, which simplifies analysis considerably compared to, for example, methods based on domain integrals that require additional post-processing. In addition to the fracture energy, cohesive zone models involve other fracture parameters, such as characteristic opening displacement and maximum cohesive tractions. It is important to obtain accurate characterization of these parameters, especially when the bulk deforms inelastically.

References

ABAQUS®, 1997. Ver. 5.7, Theory and User Manuals I, II and III, Hibbitt, Karlsson and Sorensen, 1080 Main Street, Pawtucket, RI 02860-4847, USA.

Barenblatt, G.I., 1962. The mathematical theory of equilibrium cracks in brittle fracture. In: Advances in Applied Mechanics, vol. 7, Academic Press, New York, pp. 55–129.

Bilek, Z.J., Burns, S.J., 1974. Crack propagation in wedged double cantilevered beam specimens. J. Mech. Phys. Solids 22, 85–95.

Camacho, G.T., Ortiz, M., 1996. Computational modeling of impact damage in brittle materials. Int. J. Solids Struct. 33 (20–22), 2899–2939.

Crisfield, M.A., 1997. Nonlinear Finite Element Analysis of Solids and Structures, Advanced Topics, vol. 2. Wiley, England.

Dugdale, D.S., 1960. Yielding of steel sheets containing slits. J. Mech. Phys. Solids 8, 100.

Espinosa, H.D., Zavattieri, D.P., Emore, L.D., 1998. Adaptive FEM computation of geometric and material nonlinearities with application to brittle failure. Mech. Mater. 29, 275–305.

Hilber, H.M., Hughes, T.J.R., Taylor, R., 1978. Collocation, dissipation, and 'overshoot' for time integration schemes in structural dynamics. Earthquake Engng. and Struct. Dynam. 6, 99–117.

Hutchinson, J.W., Suo, Z., 1992. Mixed mode cracking in layered materials.. Adv. Appl. Mech. 29, 63–191.

Jagota, A., Bennison, S.J., Smith, C.A., 2000. Analysis of a compressive shear test for adhesion between elastomeric polymers and rigid substrates. Int. J. Fract., in press.

Knauss, W.G., 1973. On the steady propagation of a crack in a viscoelastic sheet: experiments and analysis. In: Kausch, H.H., Jaffee, R (Eds.), Deformation and Fracture of High Polymers. Plenum Press, New York, pp. 501–541.

Nakamura, T., 1991. Three-dimensional stress fields of elastic interface cracks. J. Appl. Mech. 58, 939–946.

Needleman, A., 1990a. An analysis of tensile decohesion along an interface. J. Mech. Phys. Solids 38 (3), 289–324.

Needleman, A., 1990b. An analysis of decohesion along an imperfect interface. Int. J. Fract. 42, 21–40.

Ogden, R.W., 1984. Nonlinear Elastic Deformations. Ellis Horwood, West Sussex, England.

Rahul-Kumar, P., Jagota, A., Bennison, S.J., Saigal, S., Muralidhar, S., 1999. Polymer interfacial fracture simulations using cohesive elements. Acta Materialia 47 (15), 4161–4169.

Rahul-kumar, P., Jagota, A., Bennison, S.J., Saigal, S., 2000. Cohesive element modeling of viscoelastic fracture: application to peel testing of polymers. Int. J. Solids Struct. 37 (13), 1873–1897.

Schapery, R.A., 1975. A theory of crack initiation and growth in viscoelastic media. Int. J. Fract. 11 (1), 141–159.

Swadener, J.G., Liechti, K.M., 1998. Asymmetric shielding in mixed-mode fracture of a glass/epoxy interface. J. Appl. Mech. 65, 25–29.

Tvergaard, V., Hutchinson, J.W., 1992. The relation between crack growth resistance and fracture process parameters in elastic–plastic solids. J. Mech. Phys. Solids 40 (6), 1377–1397.

Williams, J.G., 1999. Transient effects during rapid crack propagation, Int. J. Fract. 93, 51–61.

Xu, X.P., Needleman, A., 1994. Numerical simulations of fast crack growth in brittle solids. J. Mech. Phys. Solids 42 (9), 1397–1434.

Xu, X.P., Needleman, A., 1995. Numerical simulations of dynamic interfacial crack growth allowing for crack growth away from the bond line. Int. J. Fract. 74, 253–275.

Xu, X.P., Needleman, A., 1996. Numerical simulations of dynamic crack growth along an interface. Int. J. Fract. 74, 289–324.